Cloud and Aerosol Distributions from SAGE III/ISS Observations

Mark Schoeberl[1], Eric Jensen[1],Tao Wang[2], Ghassan Taha[3,6],

Rei Ueyama [4], Yi Wang[1], Matthew DeLand[3,6], Andrew Dessler[5]

[1]Science and Technology Corporation, Columbia, MD, USA

[2] Jet Propulsion Laboratory/Caltech, Pasadena, CA, USA

[3] Science Systems and Applications, Inc., Lanham, MD, USA

[4] NASA Ames Research Center, Moffett Field, CA, USA

[5] Texas A & M, University, College Station, Texas

[6]NASA, Goddard Space Flight Center, Greenbelt, MD, USA

Corresponding Author: Mark Schoeberl, Science and Technology Corporation, 10015 Old Columbia Road, Suite E-250, Columbia, MD, 21046, USA

Key Points

- SAGE III/ISS can detect subvisible cirrus and infer the presence of visible cirrus
- Subvisible and visible cirrus are concentrated in the tropical upper troposphere
- The descending residual circulation that flanks the tropics produces reduced cloud and aerosol concentrations.

Abstract

We describe our Solar Aerosol and Gas Experiment (SAGE) III/ISS cloud detection algorithm. As in previous SAGE II/III studies this algorithm uses the extinction at 1022 nm and the extinction color ratio 520nm/1022nm to separate aerosols and clouds. We identify three types of clouds: visible cirrus (extinction coefficient $> 3x10^{-2}$ km^{-1}, subvisible cirrus (extinction $< 3x10^{-2}$ km^{-1} and $>10^{-3}$ km^{-1}), and very low extinction cloud-aerosol mixtures (extinction $< 10^{-3}$ km^{-1}). Visible cirrus cannot be quantitatively measured by SAGE because of its high extinction, but we infer the presence of cirrus through the solar attenuation of the SAGE vertical scan. We then assume that cirrus layers extend 0.5 km below the scan termination height. SAGE cirrus cloud fraction estimated this way is in qualitative agreement with CALIPSO measurements. Analyzing three years of SAGE III/ISS data, we find that visible cirrus and subvisible cirrus have nearly equal abundance in the tropical upper troposphere and the average cloud fraction is about 25%. At 16 km, the highest concentration visible cirrus and subvisible cirrus is over the Tropical West Pacific, central Africa and central South America during winter. Latitudinal gaps in zonal mean cloud fraction and average aerosol extinction apparent in the subtropical transition region are

aligned with descending branch of the residual mean circulation. We also identify four anomalous aerosol extinction periods that can be tentatively assigned to significant volcanic or fire events. Using tropopause relative coordinates, we show that maximum cloud top heights are consistently restricted to a narrow region near the tropopause.

Index Terms

0320 Cloud physics and chemistry

0341 Middle atmosphere: constituent transport and chemistry

0319 Cloud Optics

1. Introduction

High altitude clouds, especially those in the tropics (~ ±30° N-S latitude) are a regulator of climate (Zhou et al., 2014) and their abundance may be an indicator of climate change (Massie et al., 2013). Tropical cirrus near the cold point tropopause forms either through the convective injection of ice crystals or through the through slow, large-scale uplift of air into the colder tropopause region - a process that produces cirrus clouds where temperatures are coldest. Optically thin cirrus forming at the highest altitudes near the tropical tropopause signal the final dehydration of air entering the stratosphere. This cold point tropopause dehydration process, to first order, regulates stratospheric water vapor (Randel and Park, 2019 and references therein). Indeed, there is a high degree of anti-correlation between variations in cold point tropopause temperatures and cirrus cloud fraction (i.e. warmer upper tropospheric temperatures, fewer cirrus clouds; Davis et al., 2013; Wang et al., 2019; Sweeny and Fu, 2020). Modelling studies by Schoeberl et al. (2019) and Ueyama et al. (2015, 2018) had elucidated the processes that control cirrus dehydration. Cirrus produced at the boreal winter tropical tropopause layer (TTL, see Fuegistaler et al. 2009) is generated mostly through slow uplift with less direct injection of ice by convection as the altitude increases, although it is important to note that water vapor arrives at the base of the TTL layer mainly through convection (Schoeberl et al, 2019). This conceptual model explains the observed frequency of supersaturation observed in aircraft data (Jensen et al. 2017; Krämer et al., 2009, Krämer et al., 2020), and the fact that less than half the observed tropical cirrus could be traced back to low outgoing longwave radiation regions which typifies convective cores (Massie et al., 2002).

At high altitudes, cold tropical cirrus layers act like a "greenhouse cloud" (Voigt et al. 2019, Lohmann and Gasparini, 2017; Haladay and Stephens, 2009), trapping an estimated 5-6 W/m^2 of energy in the atmosphere. Modeling studies by Voigt et al, (2019) show that the net radiative forcing by these high clouds increases with increasing cloud altitude. As the climate warms, the amount of convection transporting water into the TTL may increase, as will the production of cirrus through convective detrainment. The rate of air ascent in the

TTL is also expected to increase as the Brewer-Dobson circulation accelerates in the future (Butchart, 2014 and references therein) possibly increasing the amount of stratiform cirrus. Comparative simulations by convectively resolving global models show wide disagreements on the amount of cirrus production by convection (Stevens et al., 2019), and this disagreement is due in part to the different microphysical parameterizations, nucleation models and regional differences in cirrus formation mechanisms (Patnaude et al., 2021). As noted above, dehydration by high tropical clouds regulates stratospheric water vapor (Wang et al., 2019; Randel and Park, 2019; Schoeberl et al., 2018, Jensen and Pfister, 2004, 2005) which can alter climate forcing both inside and outside the tropical regions (Forster and Shine, 1999, Solomon et al., 2010).

To summarize, tropical cirrus is an important component of the climate system through regulation of radiative forcing and stratospheric water vapor. We also note that some geo-engineering ideas involve manipulation of the incoming solar flux through changing cirrus formation rates (Lohmann and Gasparini, 2017) or the injection of aerosol clouds into the stratosphere (NASM, 2021; NRC, 2015). Cataloging the current upper troposphere/lower stratosphere (UTLS) cirrus cloud distributions before alterations are attempted would seem prudent.

In this paper we briefly review cloud observations by satellite sensors, focusing on the highest clouds detected by the SAGE III instrument on the International Space Station (SAGE III/ISS). The SAGE III/ISS standard suite of algorithms does not include a cloud product. This paper describes the evaluation of a SAGE cloud identification algorithm developed using V5.1 SAGE-III/ISS aerosol extinction coefficient profiles and shows cloud distributions from the first three complete calendar years of SAGE data.

In the next section, we describe our SAGE III/ISS cloud algorithm. This algorithm is a modified version of the algorithm described in the SAGE III Meteor ATBD for Cloud Data Products, LARC 475-00-16, 2002 (hereafter CATBD) and in Thomasson and Vernier (2013) (hereafter TV). We also briefly describe cloud particle detection by the Lidar on the Cloud–Aerosol Lidar and Infrared Pathfinder Satellite Observation (CALIPSO) satellite and the Ozone Monitoring and Profile Suite Limb Profile (OMPS- LP) instrument on the Suomi-National Polar-Orbiting Operational Environmental Satellite. These systems provide important correlative data to evaluate cloud observations from SAGE III/ISS. We then show results from applying this algorithm to the three-year SAGE III/ISS data set. The results section is followed by a summary and discussion.

2. Cloud measurements by satellite

Satellite cloud measurement instruments fall into three broad categories: Nadir imagers (e.g., MODIS, VIIRS, ABI), active radar/lidar systems (e.g., CALIPSO, CATS, CloudSat), and passive limb measurement instruments that include SAGE II/III, POAM II/III, OMPS-LP, OSIRIS, HALOE, HIRDLS, MLS, SCIAMACHY, and ACE-FTS. For brevity, these acronyms are expanded in the Appendix. Limb measurements, because of the long optical paths, are most sensi-

tive to low-extinction particle concentrations and weakly absorbing or emitting gases. Nadir active measurements are more sensitive to high extinction clouds and aerosol concentrations and provide high resolution height information along their narrow beams. Lidars have higher sensitivity to smaller cloud particles and aerosol layers than radars. They can also distinguish ice from liquids through backscatter polarization. Radars are more sensitive to larger cloud particles and can penetrate thick clouds. Nadir imagers provide wider spatial measurements, but less precise altitude information, and are also cannot detect lower extinction clouds and aerosol layers. Including SAGE, the three systems most relevant to this research are further discussed below.

2.1 SAGE II/III

The family of Stratospheric Aerosol and Gas Experiment (SAGE) II/III solar occultation instruments have provided near global cloud and aerosol information extending from 1984-2005 (Wang et al., 1996, Wang et al., 2003) and more recently from mid-2017 to the present. SAGE operates by observing the sun rising or setting through the atmospheric limb. Thus, SAGE measurements are sparse relative to other non-occultation sensors. SAGE can retrieve data with estimated vertical resolution of 0.7 km (Thomason et al., 2010), and with its ~200 km limb path, SAGE measurements are highly sensitive to the presence of optically thin cloud and aerosol layers. However, SAGE cannot make measurements in the presence of high extinction clouds such as visible cirrus, nor can it assess variations in optical extinction along the limb path. Because SAGE observes the exo-atmosphere sun either at the beginning or end of the vertical scan, SAGE is sometimes referred to as self-calibrating.

2.2 CALIPSO

The CALIPSO mission with its nadir Cloud-Aerosol Lidar with Orthogonal Polarization (CALIOP) provides two-wavelength (532 nm and 1064 nm), elastic backscatter measurements of clouds and aerosol layers, including linear polarization at 532 nm (Hunt et al, 2009; Winker et al., 2010) and provides a useful tool for evaluating SAGE cloud observations. Comparison with high-altitude aircraft lidar measurements and *in situ* measurements shows that the CALIOP standard cloud-layer detection algorithm (Vaughan et al., 2009) will not detect some optically thinner sub-visible cirrus (Davis et al., 2010).

2.3 OMPS-LP

The OMPS-LP instrument measures limb backscattered solar radiation in order to retrieve ozone and aerosols profiles. As part of the ozone retrieval algorithm, OMPS-LP team has developed a cloud height algorithm to determine where to terminate the retrieval altitude. The OMPS-LP cloud detection algorithm developed by Chen et al. (2016) utilizes the spectral dependence of the vertical radiance gradient at visible and near-IR wavelengths. The difference in radiance gradient between 674 nm and 869 nm measurements (termed radiance ratio) is used to discriminate between clouds, background aerosols, and clear sky. The algorithm flags a cloud when the difference in radiance ratio exceeds a heuris-

tically determined threshold (currently 0.15). Comparison of OMPS-LP determined cloud tops against CALIOP cloud top observations show good agreement (Chen et al., 2016). The advantage of OMPS-LP is that it makes near continuous daytime measurements and will continue to fly on future NOAA JPSS-2, JPSS-3, and JPSS-4 missions providing excellent measurement continuity.

3. SAGE III/ISS Cloud Algorithm

3.1 SAGE extinction and color ratio

Following the lidar observations reported by Sassen and Cho (1992), Wang et al. (1996) used the SAGE II extinction measurements to create a cloud classification scheme for cirrus, subvisible cirrus (SVC) and aerosols. In that scheme, aerosols have an extinction of less than $2x10^{-4}$ km^{-1} at 1020 nm; subvisible cirrus less than 0.02 km^{-1}; and cirrus extinction greater than 0.02 km^{-1} (see Table 1). Because the SAGE scan is terminated when the radiance level falls to about 0.1% of the exo-atmospheric signal, SAGE cannot provide any quantitative information on the extinction levels greater than ~0.035 km^{-1} which is typical of thicker cirrus. Wang et al. (2003) showed that the SAGE II 1020 nm extinction coefficient profile termination altitude roughly corresponded to cloud top height. They found that the zonally averaged altitude at which 50% profiles are terminated runs from ~5 km height in high in subtropical latitudes to ~11 km in the tropics.

Wang et al. (1994) and Wang et al. (2003) suggested that additional cloud information from SAGE II could be retrieved using a combination of extinction/color ratio information. A cloud height algorithm using two color ratios (525nm/1020nm and 1020/1550nm) following the Kent et al., (1997a) approach was developed for SAGE III Meteor (flown from 2001-2006). This algorithm is documented in the CATBD. Thomason and Vernier (2013; hereafter TV) developed an alternative cloud algorithm that uses one color ratio (525 nm/1020nm) and extinction at 1020 nm. The advantage of the TV algorithm is that it works with both SAGE II and SAGE III data whereas the Kent et al. algorithm uses the 1550 nm channel which was not available on SAGE II. Our tests with both algorithms indicate that they give near equivalent results.

To quantify the cloud extinction – color ratio parameters, we have performed a series of idealized experiments using the SASKTRAN radiative transfer model (Bourassa et. al., 2008) assuming spherical particles of varying size and number density. We assume the distribution of particles extends to 16 km and cuts off above to eliminate bias from layers above, then we compute the particle extinction in the 15 km tangent height layer which corresponds to path length of about 226 km.

Figure 1 shows the results of color ratio vs. extinction for our experiment and our results are similar to those reported by TV extended into smaller and larger particle domains. As particle size decreases, the color ratio increases and the extinction decreases. For very small particle sizes, we increase the concentration in order to increase the extinction and to mimic the relationship shown below in Fig. 2. The calculation shown in Fig. 1 shows how the color ratio

is helpful in distinguishing clouds from aerosols since the larger cloud particles produce extinction color ratios close to one and smaller aerosol particles produce higher color ratios as noted by Kent et al. (1997a,b). Measurements of *in situ* tropical upper tropospheric ice crystal sizes show that the concentration has a shallow peak at 1-10µm (Woods et al., 2018) and these small particles are quasi-spheroids that would have a color ratio ~1 according to Fig. 1. Aerosols in the stratosphere tend to be sub-micron (Deshler et al., 2003) and thus would exhibit a color ratio higher than ~1.5 (TV).

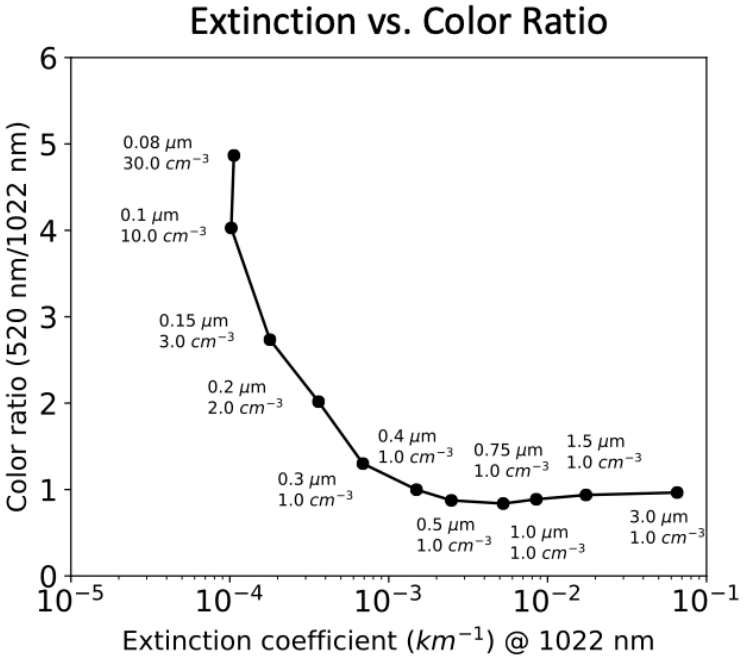

Figure 1. Results from idealized aerosol layer scattering experiment with varying number density and particle size. The particle radius in µm and number density in $cm^{-3}$are shown next to the plotted points. Color ratio increases for smaller particles and lower extinctions showing the separation of larger cloud particles from smaller aerosol particles. These results are similar to those produced by TV.

The sensor system for SAGE III/Meteor (which is the same basic instrument as SAGE III/ISS) and the L1 and L2 retrieval algorithms are detailed in the CATBD and the SAGE III Solar and Lunar Algorithm Theoretical Basis Document (LaRC Publication 475-00-109, 2002) which can be obtained from the SAGE III/ISS web site. For this study we use the 1022 and 520 nm Rayleigh scatter corrected aerosol extinction products used by TV. CATBD discusses the impact of the observing geometry and the fact that the cloud may not fill the SAGE field of view. For example, a single, small and dense cloud may produce

the same apparent extinction as a uniform low density particle layer. This is a well understood limitation of SAGE cloud measurements.

Figure 2a shows the distribution of SAGE III/ISS observations from 6/2017 to 1/2021 and the total number of profiles verses latitude within 5° latitude bins. Figure 2b shows a density diagram of the SAGE data below 20 km as a function of color ratio and extinction. There are 32,585 profiles retrieved over this period. The figure indicates the rough extinction vs color categorization of the various regions based on TV although the exact placement of the boundaries is somewhat arbitrary. The 'aerosols' regime in Fig. 2b is the same as that identified by TV. During our observing period, a number of pyrocumulonimbus (pyroCB) events occurred. These are high extinction aerosols (smoke) with a color ratio well above 1 are labeled 'aerosol plumes' in the figure. Clouds show up as extinction events with a color ratio between 0.8 and 1.2. We identify SVC as clouds with extinctions greater than 10^{-3} km^{-1} and less than 3 x 10^{-2} km^{-1} approximating Wang et al. (1997) (see Table 1). SVCs have been observed by SAGE II (Wang et al., 1996); OSIRIS (Bourassa et al., 2005); CLAES (Mergenthaler et al., 1999), CALIPSO (Martins et al. 2011, Wang et al., 2019), HIRDLS (Massie et al., 2007) and *in situ* from multiple aircraft missions (Krämer et al., 2020) and specifically during ATTREX (Woods et al. 2018) and other tropical airborne missions.

We also identify a regime with even lower cloud extinction ($< 10^{-3}$ km^{-1}). Extinctions in this region are likely optically thin cloud-aerosol mixtures (CAMs). Finally, we identify a 'visible cirrus' regime where the extinction is greater than ~3 x 10^{-2} km^{-1}. SAGE cannot measure extinction higher than 3.4 x 10^{-2} km^{-1} as noted above (the 'visible cirrus' block in Fig. 1 is nearly empty), because the SAGE scans terminate. However, knowing that the scan terminates with visible cirrus allows us to classify the termination of the scan as a cirrus event (see the CATBD). Note that the SAGE III/ISS a scan may also terminate due to ISS equipment blockage, but these events are less that 0.5% of all scans (SAGE III/ISS V5.1 Release Notes) and can be ignored. Aerosol layers are defined as regions where the 1022 nm extinction is $> 10^{-4}$ $km^{-1}$and < 5 x 10^{-3} km^{-1} with color ratio > 1.2. These criteria are summarized in Table 1.

For most cases, we expect that, as the SAGE III/ISS scan moves across the limb, the cloud will initially occupy the bottom part of the field of view, then the full field of view. Thus, we expect the extinction may be elevated when only a fraction of the cirrus cloud occupies the field of view; as a result, an SVC layer could be incorrectly reported as existing just above a cirrus cloud. In practice, we find that this type of anomaly seldom occurs.

As also noted in CATBD, the 'U' shaped limb occultation path relative to the earth surface may produce an mis-estimation of the cloud height. This occurs when higher clouds that are not located near the minimum tangent path altitude also intercept the limb field of view. These clouds could mistakenly be assigned height of the minimum tangent path altitude when they are actually taller. However, Kent et al. (1997b) showed that the assumption of clouds

occupying the other parts of the tangent path results in only a slight low bias in the retrieved extinction altitude so this effect can be neglected.

To compare SAGE III/ISS observations with OMPS-LP cloud top heights we define a cloud top height (CTH) as the first occurrence of a cloud of the types listed in Table 1 moving downward from 20 km. We note that typically aerosol are identified as extinctions with color ratios greater than 2. We have tested our algorithm using a color ratio limit of 2 instead of 1.2 and there are no noticeable differences in average aerosol extinctions shown in Figs. 8 and 9 below.

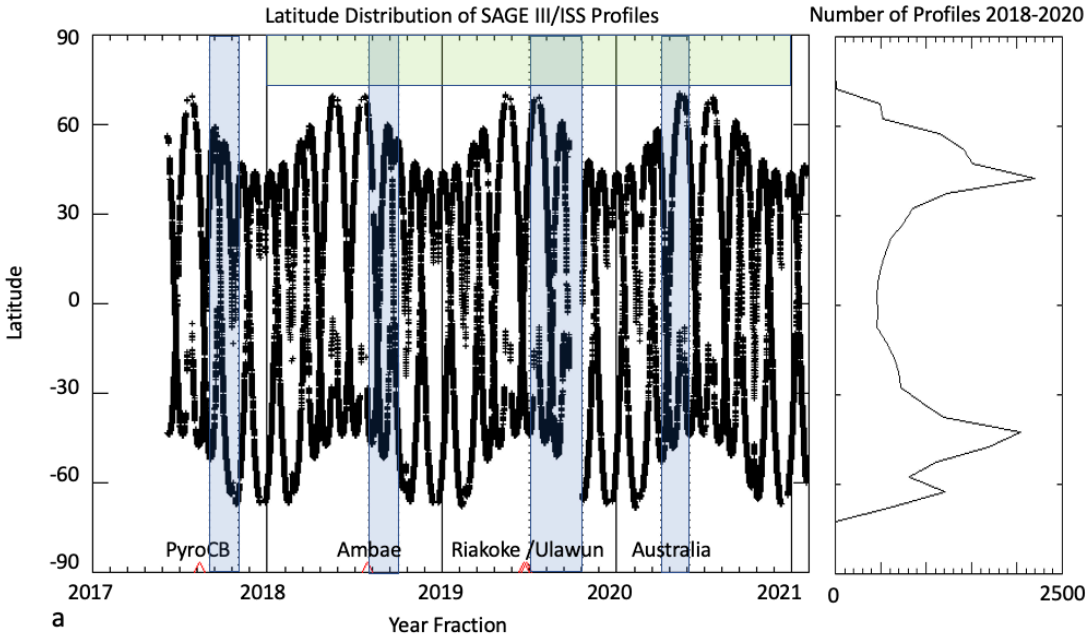

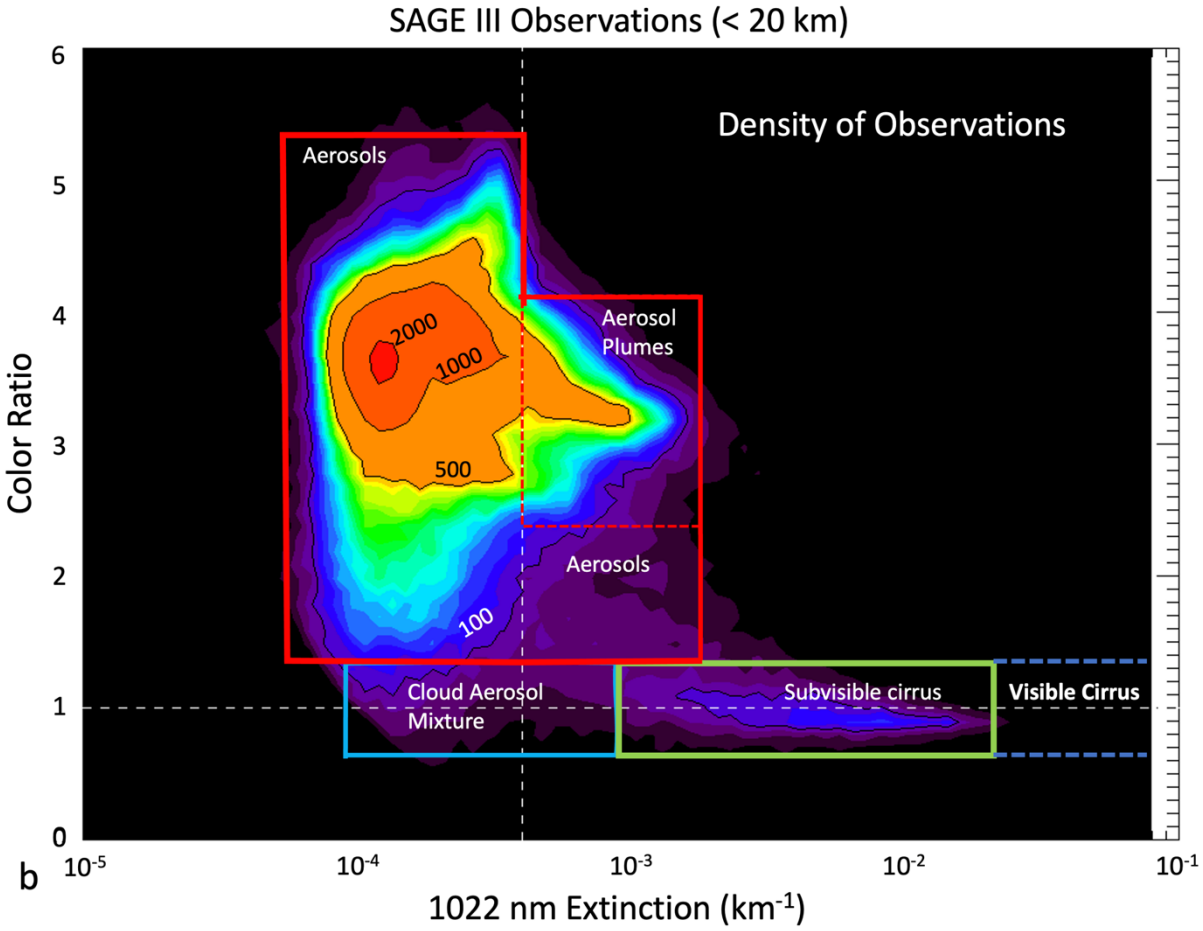

Figure 2. Part a, latitude distribution of all SAGE III/ISS measurements from 6/17/2017 through 1/31/2021. Light green domain at the top of (a) shows the 2018-2020 period used here for cloud analysis. Light blue labeled regions refer to special averaging periods for aerosol analysis shown in Fig. 9 below. Specific aerosol event sources are indicated by red triangles and labels at the bottom of figure. The number of SAGE profiles for the 2018-2020 period is shown on right using 5° latitude bins. Part b, density plot of all SAGE III/ISS observations below 20 km sorted by 1022 extinction and 520/1022 extinction (color) ratio. Data is through 1/2021. Regime classification approximately follows TV, Sassen and Cho (1993) and Wang et al. (1996). In addition, we identify low extinction cloud-aerosol mixtures. Contours show the number of measurements.

Table 1. Cloud and Aerosol Identification Criteria

Cloud Type (all < 20 km)	Wang et al. (1996)	This Paper

Table 1. Cloud and Aerosol Identification Criteria

	Extinction (km^{-1})	Extinction (km^{-1})
Visible Cirrus	$> 2 \times 10^{-2}$ km^{-1}	$> 3 \times 10^{-2}$ km^{-1}
Subvisible Cirrus (SVC)	$>2 \times 10^{-4}$ km^{-1} and $< 2 \times 10^{-2}$ km^{-1}	$> 10^{-3}$ and < 3 x
Cloud Aerosol Mixture (CAM)	$< 2 \times 10^{-4}$ km^{-1}	$>1 \times 10^{-4}$ and < 1
Aerosols	$< 2 \times 10^{-4}$ km^{-1}	$> 10^{-4}$ km^{-1} and $<$

3.2 Visible cirrus

Because SAGE is a limb viewing instrument, the optical path is ~226 km through the atmospheric limb. If the path attenuation exceeds ~0.1% of the exo-atmospheric signal, the SAGE scan data is terminated (CATBD). Fig. 3a shows 2018-2020 SAGE extinction statistics for clouds higher than 14 km divided into the SVC and CAM domains. Figure 3b shows measurements of extinction from a *in situ* ATTREX (Jensen et al., 2017) and POSIDON data along with extinction coefficient retrievals derived from the standard CALIOP layer product (Young et al., 2018; Winker et al., 2010; Young and Vaughan, 2009) as measured over the tropical west Pacific domain during boreal winter. Although, these comparisons are from quite different instruments, different sample volumes, different time periods, and are using different relative measurements, it is clear that statistics from SAGE III/ISS extinction data show the same functional form as the *in situ* measurements and CALIOP data. We note that CALIOP is starting to show reduced sensitivity for extinctions below ~3 x 10^{-3} km^{-1}.

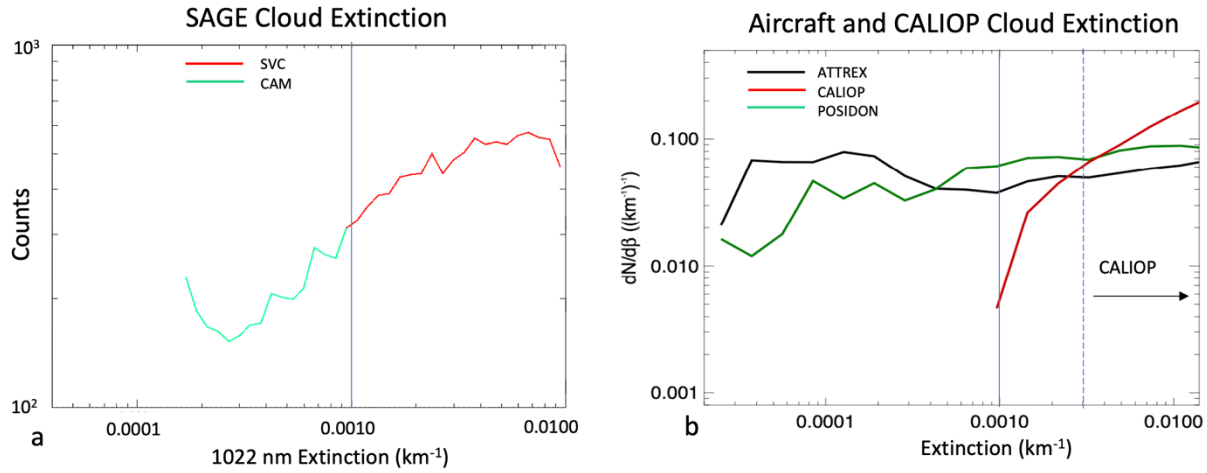

Figure 3 Part (a) 1022nm extinction distribution for all clouds 14-18 km identified by our algorithm. The distribution is cut off at 10^{-2} km^{-1} since SAGE cannot measure extinctions much above that value. The red dashed line is SVC

and the green dashed line is CAM. Part (b) shows in situ extinction measurements from NASA ATTREX and POSIDON missions, and coincident CALIOP data.

Because the SAGE scan terminates at a high extinction cloud, we can use information from CALIPSO cloud measurements to fill in the region with cirrus. This concept follows from Wang et al. (1995) where statistics of the scan termination heights were used to describe the frequency of opaque clouds. Assuming CALIPSO measures extinctions greater than ~3 x 10^{-3} km^{-1} (as shown in Fig. 3), we now assume that cirrus extends below SAGE scan termination altitude some distance. To determine that distance, we compute zonal SAGE cloud fraction that matches the extinction range of CALIOP for subvisible and visible cirrus. We then compare our SAGE cloud fraction product to CALIPSO cloud fraction data – this product is called 'SAGE/CALIOP' and includes subvisible cirrus with extinction greater than 3 x 10^{-3} km^{-1}. By varying the thickness of the added cirrus layer, we can tune the layer thickness to try and match the CALIOP cloud fraction. We find that extending the cirrus layer 1/2 km below the scan termination latitude is the best match. For these comparisons we use CALIPSO data v4.20 up to June 2020 and 4.21 July 2020-December 2020. This 1/2 km value also agrees with the results of Massie et al. (2010) who showed that the mean depth of CALIOP cirrus cloud layers is 0.5-2 km.

3.3 Cloud height retrievals

Figure 4 shows the extinction and color ratio for a single SAGE profile to illustrate the algorithm. The small colored dots at the left of each figure identify the cloud type at each scan point using the formulas in Table 1. The top altitude of each layer is also indicated. The limits used in cloud categorization are shown as vertical green lines and the MERRA2 reanalysis tropopause is shown as a horizontal blue line. If a layer cannot be identified, the altitude is set to zero. If the SAGE vertical scan terminates above 20 km then the profile is not processed.

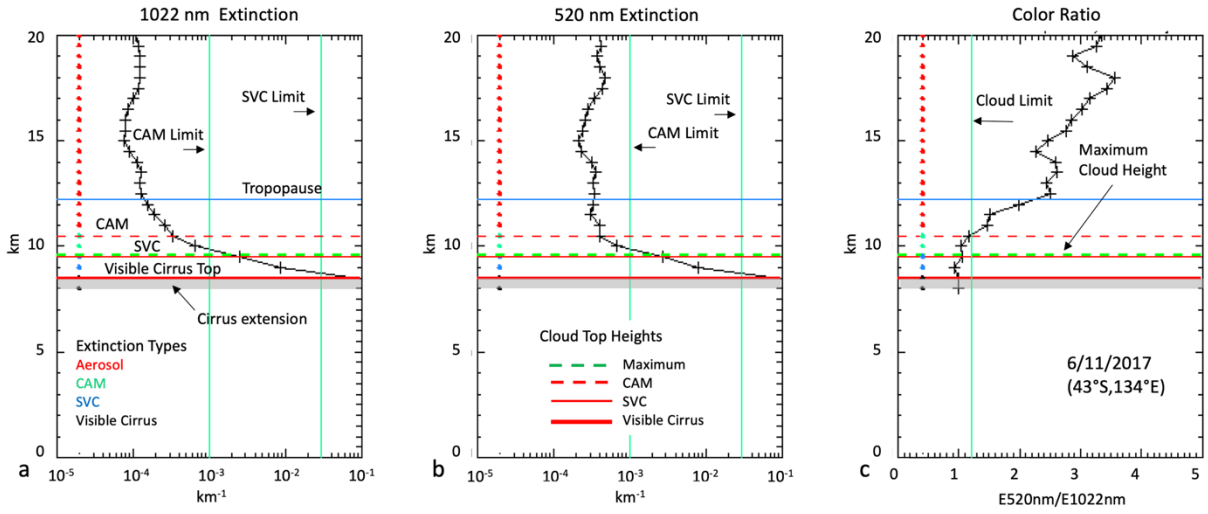

Figure 4 Clouds identification from a single example SAGE III profile on 6/11/2017 at 43°S and 134°E. Part (a) shows the extinction channel at 1022nm, part (b) is the 520 nm channel and part (c) shows the color ratio of extinction at 520nm and at 1022nm. SAGE data are crosses. The small dots to the left each figure identify the cloud type. Red is aerosol, blue is SVC, green is CAM and black is cirrus. The visible cirrus CTH is the thick solid red line, SVC height is the thin orange line, the CAM height line is a dashed line. The maximum cloud top height is the horizontal green dashed line and is the higher of either visible cirrus or SVC. The extinction limits for identifying the cloud types are shown as vertical green lines in (a) and (b); the color cloud limit is shown in (c). The blue horizontal line is the MERRA2 reanalysis tropopause. The algorithm extends cirrus ½ km below the scan termination labeled as 'cirrus extension' in the figure; the gray zone indicates visible cirrus extension.

SAGE extinction measurements cannot describe the spatial structure of the attenuators along the solar beam. In other words, a thin uniform layer of ice crystals along the 225 km path will produce the same extinction as a single isolated thick cloud. Using CALIPSO data, Massie et al. (2010) showed that the mean horizontal extent of visible cirrus sheets at 17 km is ~150-250 km and even larger at 16 km; however, the median scale for cloud anomalies is smaller. The smaller scale clouds could be associated with small scale gravity wave triggering of nucleation events (Schoeberl et al., 2015; Kim and Alexander, 2015). In short, SAGE cannot provide meaningful cloud extinction information on scales smaller than the 225 km limb path, and SAGE will underestimate the individual cloud extinction when clouds occupy only a fraction of the optical path. Thus, we will focus on cloud fraction rather than extinction. Cloud fraction is the number of cloud measurements in a volume divided by the total

number of measurements within the volume. Cloud fraction is computed on a 5° latitude by 10° longitude by ½ km grid. This horizontal scale is large enough (~500 km x 1000 km) to include the large cirrus sheets and smaller convective complexes based on the Massie et al. (2010) statistics. The long optical path will also overestimate cloud fraction compared to nadir instruments when the cloud field is patchy. Aerosol distributions, unlike clouds, tend to be more spatially uniform (except shortly after an injection event, Kar et al., 2019) and reporting average extinction measurements for aerosols is appropriate.

Lastly, to compare with OMPS-LP and CALIPSO data, we also identify the maximum cloud top height as the maximum height of either the SVC or visible cirrus layer (see Fig. 4). CAM is not used for maximum cloud top height because of its very low extinction. CAM will not be detected by either OMPS-LP or CALIPSO.

4.0 Clouds and Aerosols Observed by SAGE III/ISS

Using the algorithm described above we have processed all SAGE data from 4/2017 through 12/2020. In almost all cases we compare extinctions associated with each cloud category over the 3-year period, 2018-2020 and boreal seasonal averages over three years (June-July-August, JJA and December-January-February, DJF); the exception is the aerosol observations which are also shows for selected periods.

4.1 Cloud Fraction

Figure 5 shows the SAGE III cloud fraction based on all observations in our 3-year period and the seasonal averages. The tropopause (white line) is the average of MERRA2 tropopause heights over the same period. The MERRA2 tropopause height is approximately defined as the lowest of either the PV tropopause (3.0 PV units) or the cold point tropopause and is included in the SAGE profile data. Figure 5 and later figures also show the MERRA2 residual circulation streamlines using the formulas in Andrews et al. (1987) and Rosenlof and Holton (1993). Each streamline is generated by integrating the residual velocity for 10 days using the average residual circulation for the observing period.

Recall that we are labeling termination of the SAGE scan as a visible cirrus event with cirrus extending ½ km below the termination altitude. SVC, CAM and SAGE/CALIOP conditions are as indicated in Table 1. SAGE/CALIOP is cloud fraction as reconstructed from the SAGE data designed to include cirrus and some SVC as would be seen by CALIPSO. Fig. 5e shows the cloud fraction from CALIOP measurements over the same period. SAGE /CALIOP cloud fraction amount is in reasonable agreement with CALIOP cloud fraction. Our SAGE cloud fraction is a little low biased, and the CALIPSO cloud fraction distribution extends to a lower altitude. CALIPSO can make measurements over a deeper vertical domain, and this is the likely explanation for the cloud fraction differences between 11-13 km and the bias.

Fig. 5a, b shows that cirrus and SVC cloud fractions are comparable. The

total SAGE tropical upper tropospheric cloud fraction including cirrus, SVC and CAM (± 20°, 12-17 km) is about 25%. Within that fraction cirrus is 41%, SVC is 42%, and CAM is 17%. These statistics are consistent with those found by Martins et al. (2011) using CALIOP data although we are reporting a higher concentration of SVC than Martins et al. due likely due to the higher sensitivity of SAGE to SVC.

The seasonal distributions shown in Fig. 5f-m display similar results to the 3-year averages. In DJF, the total tropical cloud fraction is 27% and the ratio of SVC to cirrus is 1.13. For JJA, the ratio of SVC concentration relative to cirrus decreases to 0.92 and the tropical cloud fraction decreases to 23%. Part of this decrease is that the cirrus-generating Asian monsoon convection zones partially move north of the ±20° domain. The highest occurrence of SVC is in boreal winter. We see similar differences between the CALIPSO cloud fraction and the SAGE/CALIOP cloud fraction as noted above.

The overall vertical distribution of SVC shown in Fig. 5b, g, k agrees with SAGE II observations (Wang et al., 1997). In the SAGE III observations, SVC forms below the TTL base (~14 km, Fueglistaler et al., 2009) and reaches a peak where air begins to rise due to radiative heating (Schoeberl et al., 2019, Dessler et al., 2006). The rise is indicated by the residual circulation streamline divergence at about 14 km. The SVC distribution suggests a linkage to tropical convection which typically detrains at the base of the TTL. Below the base of the TTL SVC layers may be due to spreading-dissipating cirrus anvils. Above the TTL base the layers may also form in the slowly rising and cooling air, because the convective frequency above the TTL base rapidly decreases with altitude and cirrus blow off is less likely (Schoeberl et al., 2018, Ueyama et al., 2018, 2020). Convection within the TTL cannot be ruled out, however, because convection is the major source of water vapor above the base of the TTL.

The CAM cloud fraction is basically residual extinction, and because it is not a significant component, we do not display CAM distributions beyond Fig. 5c. CAM may be SVC and visible cirrus layers that are forming or dissipating; note that CAM does not extend as high as either cirrus or SVC in the tropical core.

Fig. 5 shows that the cloud fraction decreases at the edges of the tropics where the streamlines show descending air where the tropopause moves downward. This decrease in cloud fraction is also evident in the seasonal data and CALIPSO distributions. The SVC and cirrus are contained within the colder temperature zone of the TTL. The presence of visible cirrus in extra-tropical latitudes is likely result of increased land convection and frontogenesis (Ahrens, 2006).

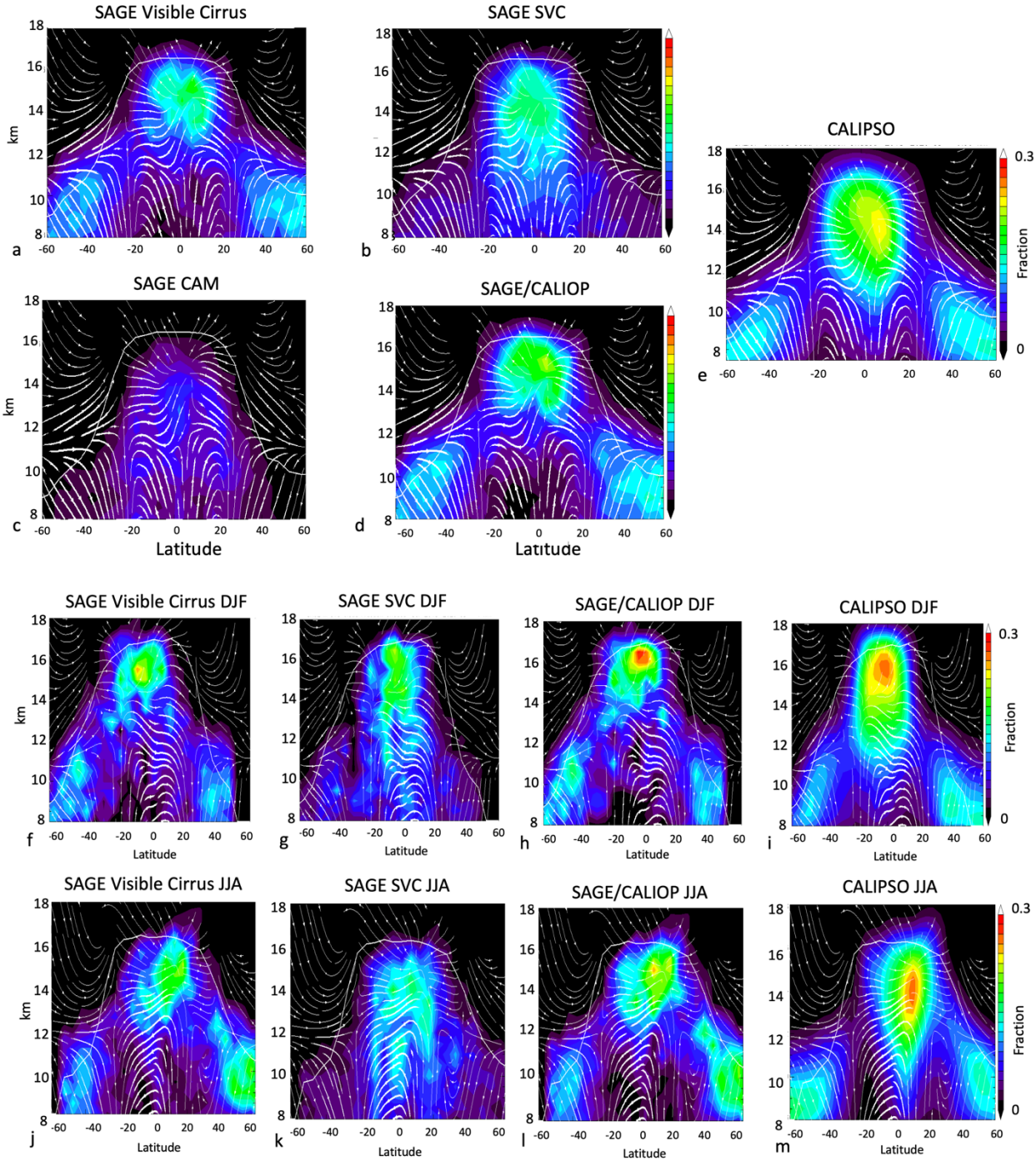
SAGE Visible Cirrus
SAGE SVC
CALIPSO
SAGE CAM
SAGE/CALIOP
SAGE Visible Cirrus DJF
SAGE SVC DJF
SAGE/CALIOP DJF
CALIPSO DJF
SAGE Visible Cirrus JJA
SAGE SVC JJA
SAGE/CALIOP JJA
CALIPSO JJA
km
Latitude
Fraction
a
b
c
d
e
f
g
h
i
j
k
l
m

Figure 5. Zonal mean distribution of CTH. Parts a-e are the three year average of the data (2018-2020). Part (a) SAGE visible cirrus, (b) SVC, (c) CAM (d) SAGE/CAL cloud fraction and (e) CALIOP cloud fraction. White line is the average tropopause height. Arrows are the period-average residual mean circulation streamlines. Parts f-m show the seasonal distributions as with parts a-e but CAM is not included. Parts f-i show the three-year averaged DJF (including Dec. 2017) and parts j-m show the JJA periods.

Figures 6 shows maps of SAGE visible cirrus, SVC, SAGE/CALIOP and CALIPSO data at 16 km – close to the tropical tropopause ~ 100 hPa. The agreement between Fig. 6c and Fig. 6d is fairly good. Both maps show the concentration of visible cirrus over the Tropical West Pacific (TWP) and the Asian Monsoon region with secondary concentrations over Africa and South America. Overall, the cloud distributions shown in Fig. 6 agree with analyses as shown in Martins et al., (2011), Massie et al. (2010, 2013), Dessler et al. (2006) and even earlier in Wang et al. (1996) although fractional definitions vary between these studies. At these altitudes, SVC has a smaller cloud fraction although the distribution is comparable. Both cirrus and SVC form in the coldest regions of the tropical troposphere.

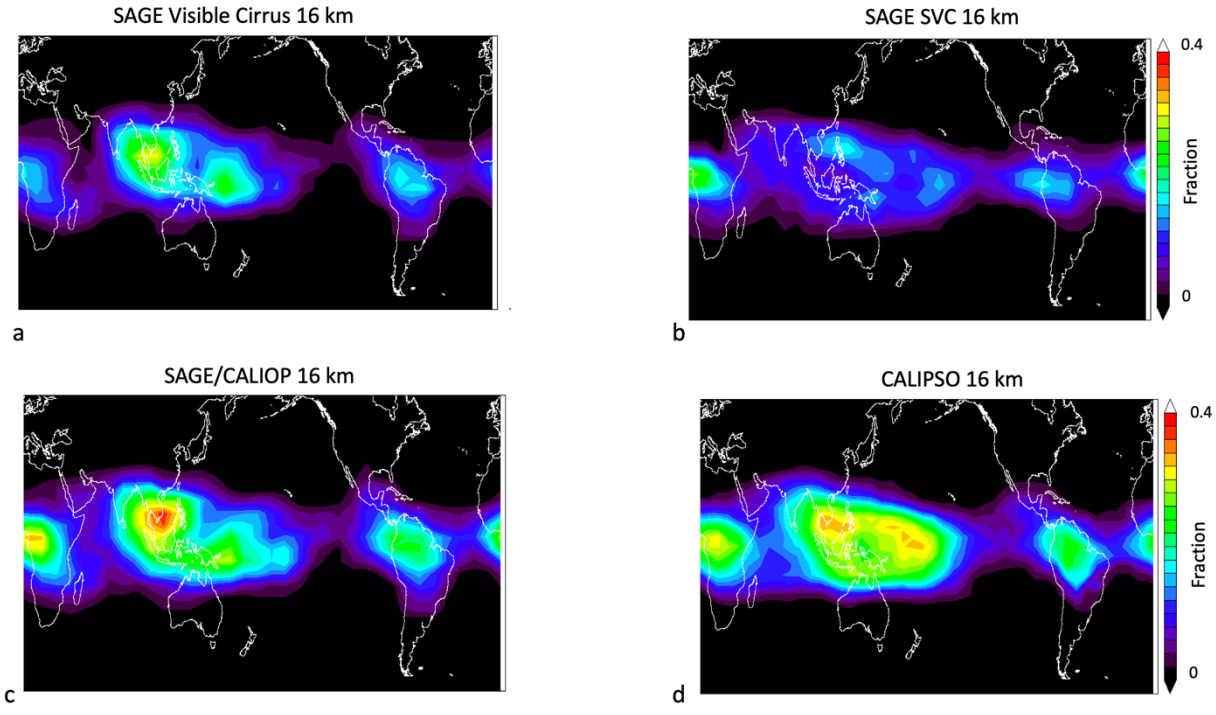

Figure 6. Cloud distribution maps at 16 km averaged over 3 years. Part (a) SAGE all cloud fraction (visible cirrus plus SVC), (b) SAGE visible cirrus, (c)

SAGE SVC , (d) CALIOP.

Figure 7 shows the seasonal variations averaged over the 3 years as in Figure 6. The SAGE DJF (Fig. 7a, b) SVC and cirrus are comparable and SAGE/CALIOP (Fig. 7c) agrees with CALIPSO (Fig. 7d). Some unusual features show up in these maps as well. For example, Fig. 7a shows a strong cirrus concentration over SE Asia extending eastward into the West Pacific, whereas SVC is more concentrated at the eastern edges of these regions. SVC is also enhanced over South America and Africa. These SVC distributions may be the result of a convective sources in the cirrus region with water vapor flowing outward forming SVC at the edges and are coincident with the relatively colder regions of the upper troposphere. During JJA, cirrus is concentrated over the monsoon regions, with smaller concentration of SVC across the Pacific.

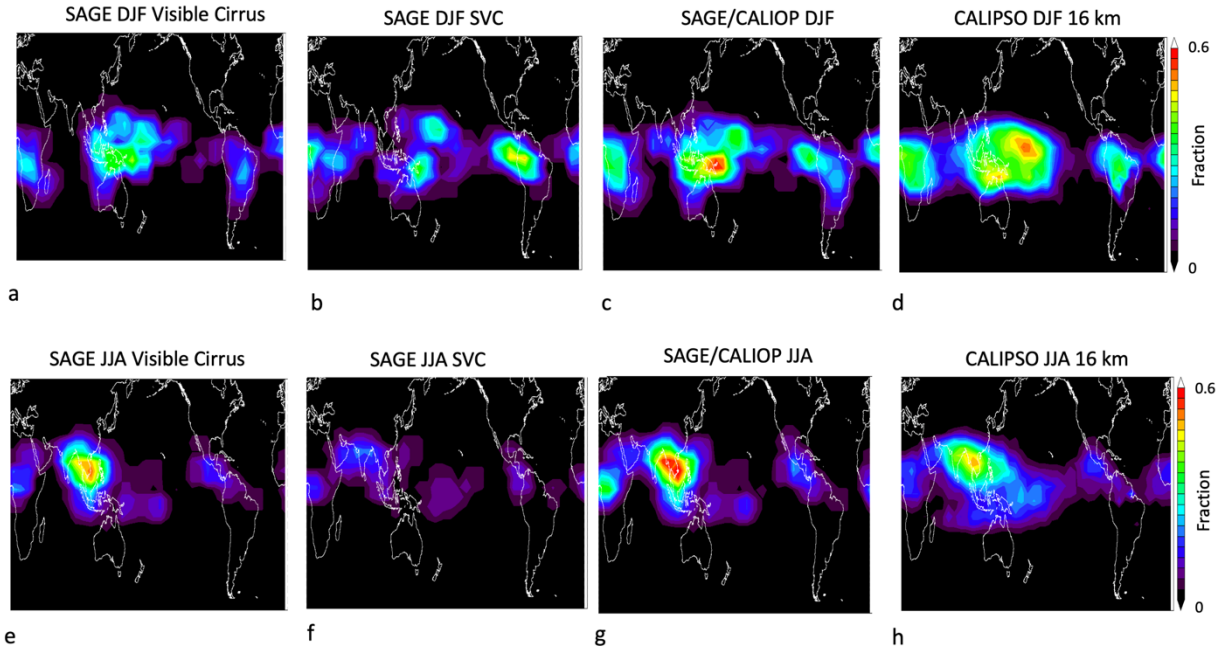

Figure 7. The 16 km seasonal cloud fraction from SAGE and CALIOP averaging 3 seasons (2018-2020). Parts a-d for DJF (including December 2017). Parts e-h for JJA. Left figures cirrus fraction, SVC is next, SAGE CALIOP is next which should be compared to CALIOP fraction on the right.

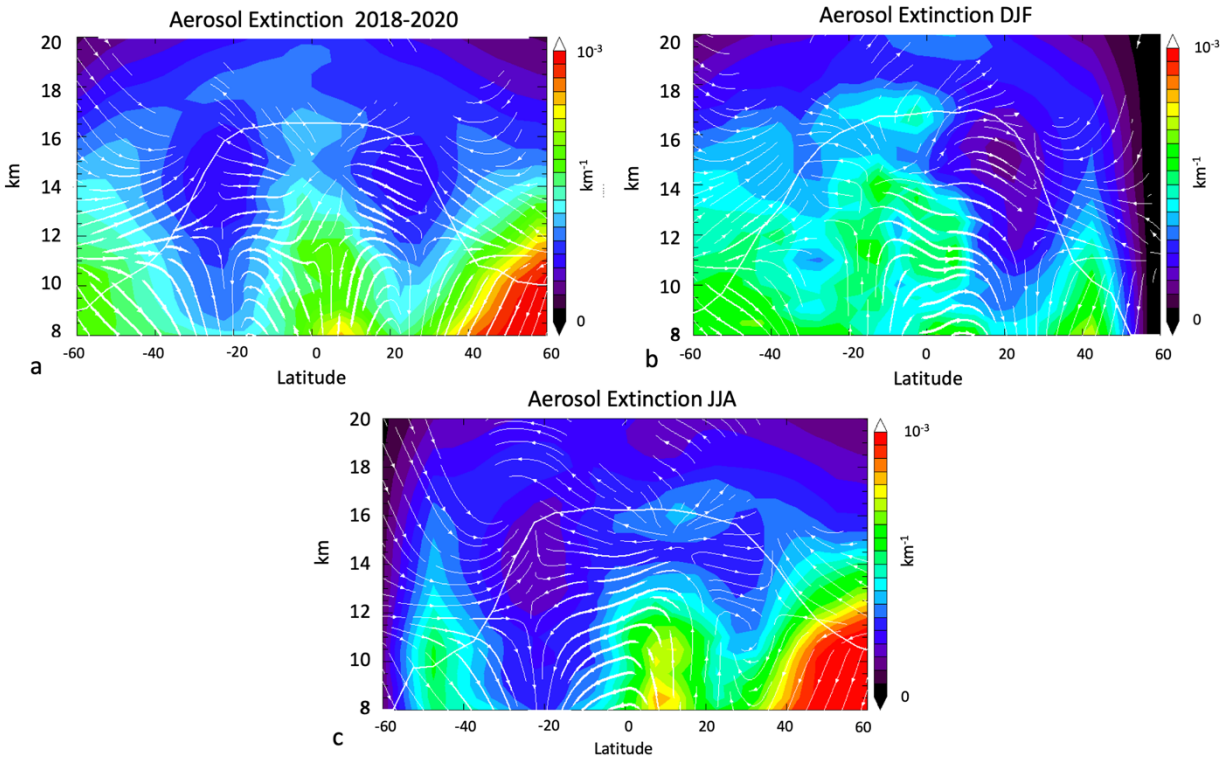

Figure 8 Part a Averaged aerosol extinction 1/2018-12/2020 using the same gridding used in Fig 5. Streamlines from Fig.5. Part b is the three year average DJF aerosol extinction with streamlines over the same period. Part c is for JJA. White line is the tropopause averaged over each period.

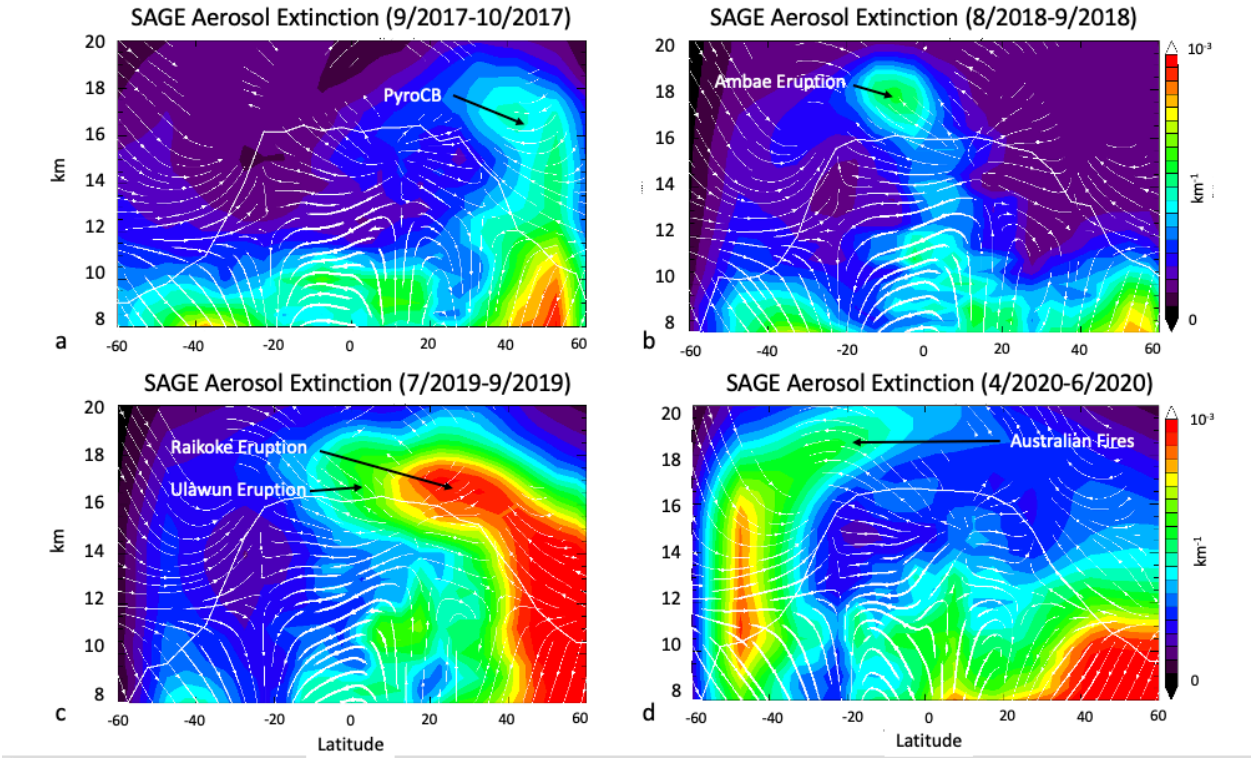

Figure 9 Averaged aerosol extinction for four periods, (a) June-Aug. 2017 (b) July-Sept. 2018, (c) July-Sept. 2019 and (d) April-June 2020 as in Fig. 8. Labels indicate the likely source of the stratospheric extinction anomalies. See Fig. 2a for the observing periods.

4.2 Aerosols

After identifying the cloud features, we can use the color ratio to isolate the aerosol distribution. Figure 8 shows the multi-year average aerosol extinction and the winter and summer periods. These results are also similar to those obtained by Thomason et al. (1997) using the longer SAGE II data record. Higher latitude aerosol distributions are more complex, but the high extra-tropical JJA tropospheric extinction levels seen in the northern hemisphere summer (Fig. 8c) are probably associated with anthropogenic emissions and fires since they show up every JJA period. Like the cloud fields, Fig. 8a shows that, there are lower extinction regions bracketing the tropics which have also been observed in the SAGE II data (TV). These are regions of descending air as indicated by the residual circulation streamlines. The impact of the descending circulation is more dramatic in the seasonal averages (Figs. 8b,8c) as might be expected.

The multi-year average shown in Fig. 8 smooths out the seasonal extinction anomalies which show considerable structure. Figure 9 shows four shorter pe-

riods with distinct aerosol extinction anomalies, the specific SAGE locations averaged into these periods are shown if Fig. 2a. In Figure 8a, the boreal polar lower stratosphere is enhanced by the frequent pyrocumulonimbus (pyroCB) events that occurred in North America and Siberia during the summer 2017 (Torres et al., 2020). The summer lower stratospheric residual circulation streamlines show how pyroCB aerosols are lofted into the stratosphere and radiative heating of the aerosol can increase the ascent rate (Yu et al., 2021). The pattern in this figure roughly agrees with the CALIPSO aerosol 532 nm scattering ratio from a slightly later period (Fig. 9, Kar et al., 2019). Figure 9b shows a significant tropical aerosol enhancement likely produced by the eruption of the volcano on Ambae island (15°S, 167°E) on July 28, 2018. This volcano produced are record amount of SO_2 and the plume reached the lower stratosphere. The Ambae aerosol plume is clearly visible in the upper tropical troposphere despite the presence of clouds in this region confirming our algorithm for separating clouds from aerosols (Kloss et al., 2020). The Brewer-Dobson circulation over the equator is carrying the plume into the lower tropical stratosphere as shown in the residual streamlines. On June 21, 2019, the Raikoke volcano (48°N, 153°E) erupted sending a large plume into the stratosphere that is the likely the primary source of the extinction enhancement seen in Figure 9c. The eruption of Ulawun (5°S, 151°E) on June 26, 2019 contributed to the aerosol enhancement is the southern hemisphere (Kloss et al., 2021). Fig. 9c is similar to the average extinction plot in Park et al. (2021, Fig. 3). OMPS-LP measurements of the aerosol plume are consistent with the SAGE extinction enhancement (Kloss et al., 2021; Gorkavyi et al., 2021). Again, the stratospheric summer circulation guides this plume from higher latitudes toward the tropics and higher altitude. Finally, Fig. 9c shows the smoke from the severe Australian fires produced a significant extinction anomaly in the spring of 2020. The stratospheric circulation appears counter the advection of this anomaly (flow is downward, but plume is moving upward). However, there is strong evidence that this plume self-lofted into the stratosphere (Yu et al., 2021; Khaykin et al, 2020; Schwarz et al., 2020) and our aerosol enhancement is consistent with that conclusion.

4.3 Cloud Top Heights

Cloud top height (CTH) is an important diagnostic of the last occurrence of saturation and dehydration for air parcels moving upward from the tropical upper troposphere to the stratosphere. As noted above, the CTH computed from the SAGE profiles is the maximum cloud top height for each SAGE cloud distribution. Thus, the occurrence of visible cirrus cloud tops will be concentrated in the upper troposphere and the distribution will be weighted as such compared to the cloud fraction. For the 'all CTH' we compute the higher of either visible cirrus or SVC. CALIOP CTH distributions over the same period provide a useful comparison for high clouds (Martins et al., 2011; Massie et al., 2010; Sassen et al. 2008).

Figure 10 shows zonal cross sections of the CTH fraction using the same griding as Fig. 5; the white line is that ensemble average tropopause height. The SAGE

CTH visible cirrus, and SVC (Fig. 10 b, c) show similar correspondence with Figs. 5a,b. CTH will show a lower concentration than cloud fraction because there is only one CTH for each cloud type in a profile. Figure 10a shows that the SAGE CTH agrees with the CALIOP CTH distribution (Fig. 10d) noting that SAGE sees more SVC than CALIOP. Figure 11 shows the distribution of cloud top height fraction at 16 km and can be compared with Fig. 6. The SAGE results are in reasonable agreement with CALIOP measurements, and again we note that our SAGE algorithm will also flag SVC which will increase the concentration of CTHs (compare Fig. 11a with Fig. 11d).

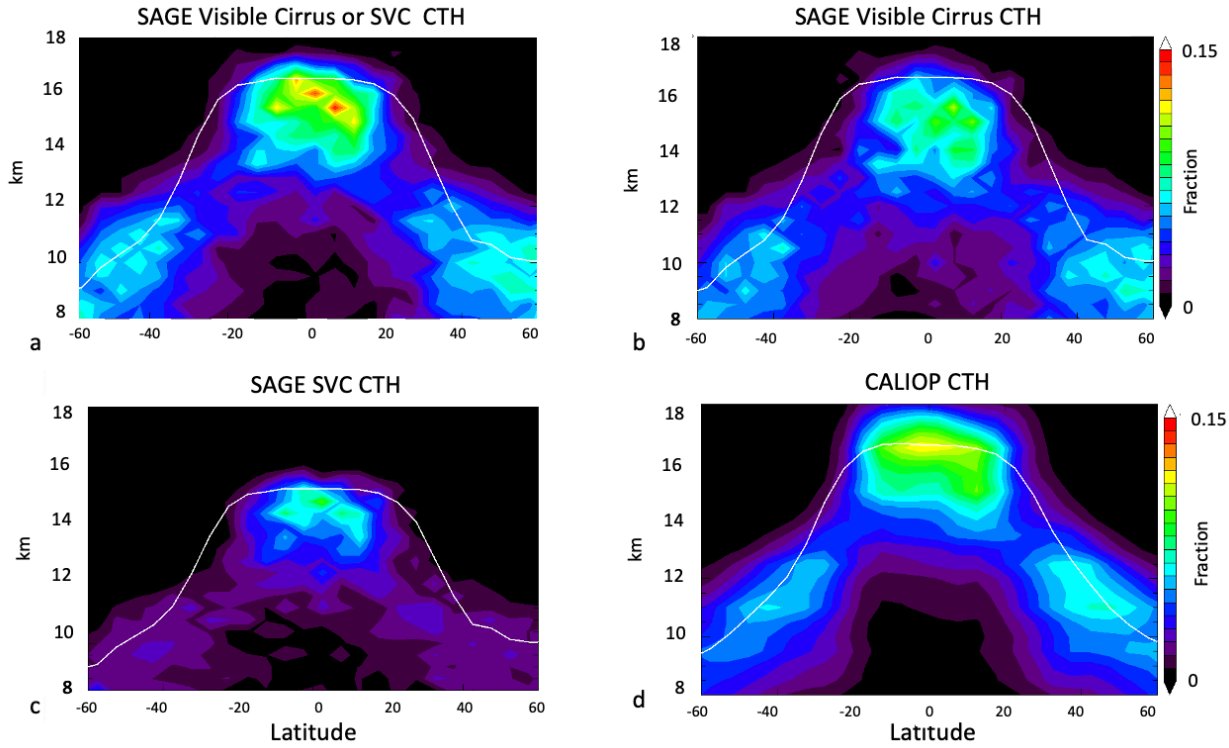

Figure 10 Cloud top occurrence fraction over 2018-2020 period. Part (a) maximum of either visible cirrus or SVC clouds, part (b) visible cirrus and part (c) SVC and part (d) CALIOP. The white line is the ensemble average tropopause height at the same latitude grid.

Note that the CTH distribution in Fig. 10 appears to extend slightly above the tropopause.

This extension CTH above the tropopause is partly due the variation in tropopause with longitude and time over our averaging period. This variation lowers the average tropopause height relative to higher clouds at some other longitudes. To reduce this variability, we can compute the cloud fraction in

tropopause relative coordinates (e.g. Pan and Munchak, 2011). We subtract the MERRA2 tropopause height from the cloud top height and then align the distribution with the zonal mean tropopause. The results for SAGE data are shown in Figure 12a,b . Shifting to tropopause relative coordinates shows that SAGE all cloud and SVC distribution now basically hugging the tropopause in the tropics and extra-tropics and CTHs extend above the tropopause in a layer no thicker than 1 km. Figure 12c shows the CALIPSO CTH relative to the tropopause height and should be compared to Fig. 10d.

At this point we introduce OMPS-LP CTH for comparison. As described in Section 2.3, polar orbiting OMPS-LP on the Suomi NPP satellite produces daytime CTH measurements (Chen et al., 2016). Because of the long path length and OMPS-LP could be more sensitive to thin clouds than CALIPSO. However, OMPS-LP data has not been examined for sensitivity to SVCs although the potential for detection of SVCs by this type of limb scattering instrument exists (Bourassa et al., 2005). We removed polar stratospheric cloud and thick aerosol anomalies that occasionally trigger the cloud height algorithm from the OMPS-LP cloud height data set. Figure 11d shows the OMPS-LP data. Compared to Fig 12a, the plots show good agreement with the SAGE data with each other.

All three data sets show a slight extension of cloud top heights above the tropopause as noted above. The OMPS-LP data is reported every 1 km, SAGE, every ½ km and our CALIOP profiles are averaged into ½ km bins. The MERRA2 vertical resolution is ~0.5 km at the tropical tropopause (GMAO office Note No. 9, MERRA-2: File Specification). Thus, the extension of the CTH distribution above the tropopause may simply be a result of tropopause location uncertainty. As noted above, cloud height measurement uncertainty exists as well. We also note that overshooting convection carries the tropopause upward and this temporary upward extension of the tropopause will not be evident in the lower spatial resolution MERRA2 data; thus, CALIOP cloud locations might appear to be above the tropopause when they are not. Given the uncertainty in the tropopause height and vertical resolution of SAGE and OMPS instruments, the evidence of extensive cirrus formation occurring above the tropopause is tenuous. Further exploration the near-tropopause cloud formation is beyond the scope of this paper.

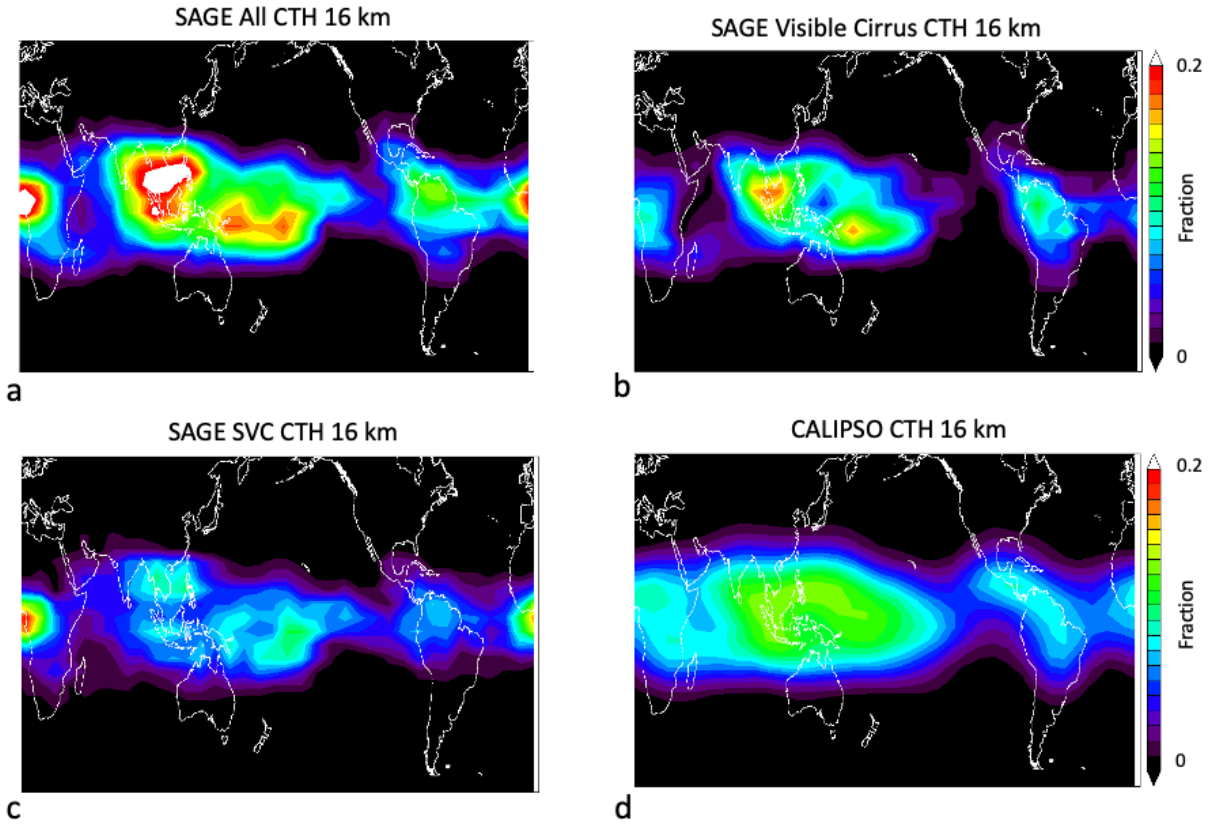

Figure 11 Cloud top height fraction maps occurrence at 16 km over 2018-2020 period. Part (a) SAGE max CTH, part (b) SAGE visible cirrus and part (c) SAGE SVC (d) CALIPSO cloud top heights.

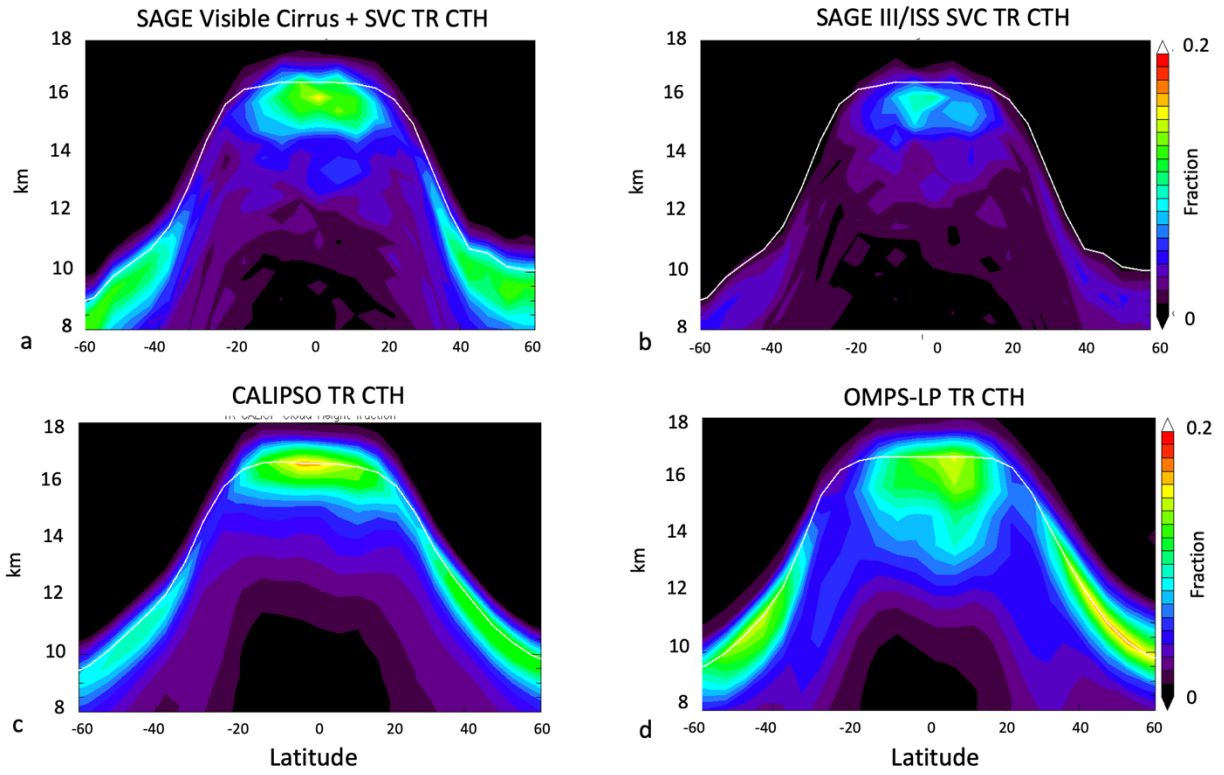

Figure 12 Cloud top height fraction maps occurrence relative to the tropopause. Part (a) maximum SAGE CTH, part (b) SAGE SVC, part (c) CALIPSO CTH and part (d) OMPS-LP CTH

5.0 Summary and Discussion

We have a developed a SAGE III/ISS cloud algorithm that uses extinction and color ratio (extinction at 520 nm /extinction 1022 nm) to infer the presence of visible cirrus, identify subvisual cirrus (SVC) and low extinction cloud-aerosol mixtures (CAM). Our approach follows the work of Thomason and Vernier (2013) and the SAGE III CATBD. The color ratio limits for clouds that we have chosen (0.8-1.2) matches that expected from Mie theory for larger particles characteristic of ice crystals. Extinction measurements used here are the SAGE III/ISS, Rayleigh scatter corrected, aerosol extinction profiles.

SAGE cannot measure extinctions higher than roughly ~$3x10^{-2}$ km^{-1} but is sensitive to extinction values down to 10^{-4} km^{-1} which includes aerosols and SVC. CALIOP, by comparison, can measure extinctions greater than $3x10^{-2}$ km^{-1} but the standard product does not identify clouds with extinctions lower than about ~$3x10^{-3}$ km^{-1}. SAGE terminates its vertical scan for average path extinctions greater than ~$3x10^{-2}$ km^{-1} (CATBD) and our retrieval scheme assumes that this is due to the presence of visible cirrus as discussed by Wang et al., (1995). We

then assume that a visible cirrus layer extends to a depth of 1/2 km below the scan termination. This depth was determined by comparing the SAGE cloud fraction measured over the CALIOP extinction range to the CALIPSO cloud fraction. We also determines the highest occurrence of each cloud type in the SAGE profile and the maximum cloud altitude for whichever is higher, either visible cirrus or SVC, and use our color ratio/ extinction discriminator to assess aerosol extinction.

We have generated cloud fraction and cloud top height statistics for three years of SAGE III/ISS data, 2018-2020. The highest concentration of these two cloud types is seen below the tropical tropopause as shown in the cloud fraction figures, and cloud height data in tropopause relative coordinates. In the summer, the maximum visible cirrus abundance is centered over the Asian monsoon region and the relative abundance of SVC is lower (Fig. 5f, 5i). In winter, SVC and visible cirrus abundance reaches a maximum in the upper tropical tropopause consistent with current theories of the cloud-formation/ dehydration process (Schoeberl et al., 2019; Ueyama et al., 2015, 2018 and references therein).

Visible cirrus and SVC have near equal average abundance in the tropics ($\pm 20°$), and we estimate that cirrus and SVC comprise ~25% total cloud fraction above 12 km as averaged over three years of SAGE data. This total abundance is slightly higher in boreal winter. The overall pattern of cloud abundance is consistent with previous studies (Martins et al., 2011; Massie et al. 2010, 2013; Dessler et al., 2006; Wang et al., 1996). Using tropopause relative coordinates, we find an abrupt decrease in cloud top height fraction crossing from the troposphere to the stratosphere with a cloud layer fraction maxima roughly centered on the tropopause. Comparing our results with CALIPSO and OMPS-LP cloud heights, we show good agreement between these data sets.

Overplotting the residual circulation streamlines shows cloud fraction gaps in the zonal mean fields between the tropics and extra-tropics. These gaps are co-located with regions of descending air. Both SVC and visible cirrus have the largest concentration in the tropics with the highest cloud fraction near the base of the TTL (~14 km). This is the altitude for the peak of occurrence of tropical convective detrainment, and transition to radiatively heated ascending air within the TTL region. SVC within the TTL is likely the result of a combination of stratiform cirrus that nucleates in the ascending/cooling air, and decaying anvils from convective towers. Little SVC is found below 11 km consistent with the decaying anvil hypothesis as the primary source below the TTL.

Aerosol 1022 nm extinction measurements (color ratios > 1.2) show strong anomalies associated with volcanic and fire events, and we have tentatively assigned causes for these anomalies. Latitudinal minima in the aerosol average extinction also are seen and, like the gaps in the cloud fields, these are co-located with the descending residual circulation at the edges of the tropics.

Although the frequency of SAGE III/ISS measurements is much lower than OMPS-LP or CALIPSO, the high sensitivity of SAGE measurements to low

extinction clouds shows that these measurements complement OMPS-LP and CALIPSO. We have also shown that SAGE scan termination altitude provides useful information about the frequency of higher extinction cirrus clouds and this information can be used to extend the SAGE measurements.

Acknowledgements

This work was funded by NASA grants 80NSSC19K0757 and 15-CCST15-0098.

All the data sets used in this study are from NASA and can be downloaded at no cost.

The SAGE III /ISS data is available at https://asdc.larc.nasa.gov/project/SAGE%20III-ISS

DOI: 10.5067/ISS/SAGEIII/SOLAR_HDF4_L2-V5.1

CALIPSO data release 4 is available at https://asdc.larc.nasa.gov/data/CALIPSO/ . OMPS-LP data is archived at the Goddard Disc, https://disc.gsfc.nasa.gov/datasets/OMPS_NPP_LP_L2_O3_DAILY_2/summary?keywords=OMPS_NPP_LP_L2_O3_DAILY_2).

The authors would also like to thank Dr. Wandi Yu for processing MERRA2 data, John Kummer for initial work on the SAGE III data set, and Dr. Melody Avery for many helpful comments and discussions

Appendix

Satellite instrument acronyms not expanded in the paper.

ABI – Advanced Baseline Imager

ACE-FTS – Atmospheric Chemistry Experiment – Fourier Transform Spectrometer

CATS – Cloud Aerosol Transport System

HALOE – Halogen Limb Occultation Experiment

HIRDLS - High Resolution Dynamics Limb Sounder

MLS – Microwave Limb Sounder

MODIS – Moderate Resolution Imaging Spectroradiometer

OSIRIS - Optical Spectrograph and Infrared Imager System

POAM – Polar Ozone and Aerosol Measurement

SCIAMACHY - Scanning Imaging Absorption Spectrometer for Atmospheric Chartography

VIIRS – Visible Infrared Imaging Radiometer Suite

References

Ahrens, C. D. (2006). Meteorology Today: An Introduction to Weather, Climate, and the Environment (8 ed.). Brooks Cole. ISBN 978-0-495-01162-0. OCLC 693475796.

Andrews, D. G., J. R. Holton, and C. B. Leovy (1987). Middle Atmosphere Dynamics, vol. 40, Academic Press, San Diego, 489 pp.

Borrmann, S., Kunkel, D., Weigel, R., Minikin, A., Deshler, T., Wilson, J. C., Curtius, J., Volk, C. M., Homan, C. D., Ulanovsky, A., Ravegnani, F., Viciani, S., Shur, G. N., Belyaev,

G. V., Law, K. S., and Cairo, F. (2010). Aerosols in the tropical and subtropical UT/LS: in-situ measurements of submicron particle abundance and volatility, Atmos. Chem. Phys., 10, 5573–5592, doi:10.5194/acp-10-5573-2010.

Bourassa, A., Degenstein, D., and Llewellyn, E. (2005). Climatology of the subvisual cirrus clouds as seen by OSIRIS on Odin, Adv. Space Res., 36, 807–812, doi:10.1016/j.asr.2005.05.045

Bourassa, A.E., Degenstein, D.A. and Llewellyn, E.J. (2008). SASKTRAN: A spherical geometry radiative transfer code for efficient estimation of limb scattered sunlight. Journal of Quantitative Spectroscopy and Radiative Transfer, 109(1), pp. 52-73

Butchart, N. (2014), The Brewer-Dobson circulation, Rev. Geophys., 52, 157–184, doi:10.1002/2013RG000448.

Chen, Z., DeLand, M., and Bhartia, P. K., (2016) A new algorithm for detecting cloud height using OMPS/LP measurements, Atmos. Meas. Tech., 9, 1239-1246, doi:10.5194/amt-9-1239-2016.

Davis, S. M., C. K. Liang, and K. H. Rosenlof (2013), Interannual variability of tropical tropopause layer clouds, J. Geophys. Res. Lett., 40, 2862–2866, doi:10.1002/grl.50512.

Deshler, T., M. E. Hervig, D. J. Hofmann, J. M. Rosen, and J. B. Liley, (2003). Thirty years of *in situ* stratospheric aerosol size distribution measurements from Laramie, Wyoming (41°N), using balloon-borne instruments, J. Geophys. Res., 108(D5), 4167, doi:10.1029/2002JD002514

Dessler, A. E., Palm, S. P., & Spinhirne, J. D. (2006). Tropical cloud-top height distributions revealed by the Ice, Cloud, and Land Elevation Satellite (ICESat)/Geoscience Laser Altimeter System (GLAS). *Journal of Geophysical Research, 111*, doi:10.1029/2005JD006705

Forster, P. N. and K. Shine (1999), Stratospheric water vapour changes as a possible contributor to observed stratospheric cooling, Geophys. Res. Lett, 26, 3309-3312.

Fueglistaler, S., A. E. Dessler, T. J. Dunkerton, I. Folkins, Q. Fu, and P. W. Mote (2009). The tropical tropopause layer, in Rev. Geophys., edited, p. 10.1029/2008RG000267.

Gettelman, A., X. Liu, D. Barahona, U. Lohmann, and C. Chen (2012). Climate impacts of ice nucleation, J. Geophys. Res., 117, D20201, doi:10.1029/2012JD017950.

Gorkavyi, N., N. Krotkov, C. Li, L. Lait, P. Colarco, S. Carn, M. DeLand, P. Newman, M. Schoeberl, G. Taha, O. Torres, Al. Vasilkov, J. Joiner, (2021). Tracking aerosols and SO_2 clouds from the Raikoke eruption: 3D view from satellite observations. Atmos Chem. Phys. Disc., https://doi.org/10.5194/amt-2021-58

Haladay, T., and G. Stephens (2009). Characteristics of tropical thin cirrus clouds deduced from joint CloudSat and CALIPSO observations, J. Geophys. Res., 114, D00A25, doi:10.1029/2008JD010675.

Jensen, E., and L. Pfister (2004). Transport and freeze-drying in the tropical tropopause layer, J. Geophys. Res., 109, D02207, doi:10.1029/2003JD004022.

Jensen, E., & L. Pfister (2005). Implications of persistent ice supersaturation in cold cirrus for stratospheric water vapor, Geophys. Res. Lett., 32, L01808, doi:10.1029/2004GL021125.

Jensen, E., L. Pfister, T. Bui, P. Lawson, and D. Baumgardner (2010). Ice nucleation and cloud microphysical properties in tropical tropopause layer cirrus, *Atmos. Chem. Phys.*, **10**(3), 1369– 1384.

Jensen, E. J., et al., (2017). The NASA Airborne Tropical Tropopause Experiment: High-Altitude Aircraft Measurements in the Tropical Western Pacific, Bull. Amer. Meteor. Soc., 98, 129-143, doi:10.1175/BAMS-D-14-00263.1

Kar, J., K.-P. Lee, M. A. Vaughan, J. L. Tackett, C. R. Trepte, D. M. Winker,

P. L. Lucker1, and B. J. Getzewich, (2019). CALIPSO level 3 stratospheric aerosol profile product: version 1.00 algorithm description and initial assessment, Atmos. Meas. Tech., 12, 6173–6191, https://doi.org/10.5194/amt-12-6173-2019.

Kent, G. S., P-H. Wang, and K. M. Skeens, (1997a). Discrimination of cloud and aerosol in the Stratospheric Aerosol and Gas Experiment (SAGE III) occultation data, *Appl. Opt.*, 33, 8639-8649.

Kent, G. S., D. M. Winker, M. A. Vaughan, P-H. Wang, and K. M. Skeens, (1997b). Simulation of SAGE II cloud measurements using airborne lidar data. *J. Geophys. Res.*, 102, 21,795-21,807

Khaykin, S., Legras, B., Bucci, S. et al. (2020). The 2019/20 Australian wildfires

generated a persistent smoke-charged vortex rising up to 35 km altitude. Commun.

Earth Environ,. 1, 22, https://doi.org/10.1038/s43247-020-00022-5

Kim, J.-E., and M. J. Alexander (2015). Direct impacts of waves on tropical cold point tropopause temperature, Geophys. Res. Lett., 42, 1584–1592, doi:10.1002/2014GL062737.

Kloss, C., Sellitto, P., Legras, B., Vernier, J.P., Jégou, F., Venkat, Ratnam, M., et al. (2020). Impact of the 2018 Ambae eruption on the global stratospheric aerosol layer and climate. J. Geophys. Res.: Atmospheres, 125, e2020JD032410. https://doi.org/10.1029/2020JD032410.

Kloss, C., Berthet, G., Sellitto, P., Ploeger, F., Taha, G., Tidiga, M., Eremenko, M., Bossolasco, A., Jégou, F., Renard, J.-B., and Legras, B.(2021), Stratospheric aerosol layer perturbation caused by the 2019 Raikoke and Ulawun eruptions and their radiative forcing, Atmos. Chem. Phys., 21, 535–560, https://doi.org/10.5194/acp-21-535-2021.

Krämer, M. et al., (2020) A microphysics guide to cirrus – Part 2 (2020). Climatologies of clouds and humidity from observations, Atmos. Chem. Phys., 20, 12569–12608 https://doi.org/10.5194/acp-20-12569-2020

Lohmann, U. and B. Gasparini (2017). A cirrus cloud climate dial? Science, 357, 248-249

DOI: 10.1126/science.aan3325.

Martins, E., V. Noel, and H. Chepfer (2011). Properties of cirrus and subvisible cirrus from nighttime Cloud-Aerosol Lidar with Orthogonal Polarization (CALIOP), related to atmospheric dynamics and water vapor, J. Geophys. Res., 116, D02208, doi:10.1029/2010JD014519

Massie, S., A. Gettelman, W. Randel, and D. Baumgardner, (2002). Distribution of tropical cirrus in relation to convection, J. Geophys. Res., 107(D21), 4591, doi:10.1029/2001JD001293.

Massie, S., et al. (2007). High Resolution Dynamics Limb Sounder observations of polar stratospheric clouds and subvisible cirrus, J. Geophys. Res., 112, D24S31, doi:10.1029/2007JD008788.

Massie, S. T., J. Gille, C. Craig, R. Khosravi, J. Barnett, W. Read, and D. Winker (2010). HIRDLS and CALIPSO observations of tropical cirrus, J. Geophys. Res., 115, D00H11, doi:10.1029/2009JD012100

Massie, S. T., R. Khosravi, and J. C. Gille (2013). A multidecadal study of cirrus in the tropical tropopause layer, J. Geophys. Res. Atmos., 118, 7938–7947, doi:10.1002/jgrd.50596.

Mergenthaler, J., A. Roche, J. Kumer, and G. Ely (1999). Cryogenic limb array etalon spectrometer observations of tropical cirrus, J. Geophys. Res., 104,

22183–22194, doi:10.1029/1999JD900397.

Meyer, K., and S. Platnick (2010). Utilizing the MODIS 1.38 mm channel for cirrus cloud optical thickness retrievals: Algorithm and retrieval uncertainties, J. Geophys. Res., 115, D24209, doi:10.1029/2010JD014872.

NRC - National Research Council (2015) Climate Intervention: Reflecting Sunlight to Cool Earth. Washington, DC: The National Academies Press. https://doi.org/10.17226/18988.

NASEM - National Academies of Sciences, Engineering, and Medicine (2021) Reflecting

Sunlight: Recommendations for Solar Geoengineering Research and Research Governance. Washington, DC: The National Academies Press. https://doi.org/10.17226/25762.

Pan, L. L., and L. A. Munchak (2011). Relationship of cloud top to the tropopause and jet structure from CALIPSO data, J. Geophys. Res., 116, D12201, doi:10.1029/2010JD015462.

Park, M., W. J Randel, R. P. Damadeo, D. E. Flittner, S. M., Davis, K. H. Rosenlof,

et al. (2021). Near-global variability of stratospheric water vapor observed by SAGE III/ISS. Journal of Geophysical Research: Atmospheres, 126, e2020JD034274. https://doi.

org/10.1029/2020JD034274

Patnaude, R. M. Diao, X. Liu and S. Chu (2021). Effects of thermodynamics, dynamics and aerosols on cirrus clouds based on in situ observations and NCAR CAM6, Atmos. Chem. Phys., 21, 1835–1859, https://doi.org/10.5194/acp-21-1835-2021

Randel, W. and E. Jensen (2013), Physical processes in the tropical tropopause layer and their roles in a changing climate, Nat. Geoscience, 6, DOI: 10.1038/NGEO1733

Randel, W., and Park, M. (2019). Diagnosing observed stratospheric water vapor relationships to the cold point tropical tropopause. Journal of Geophysical Research: Atmospheres, 124, https://doi.org/10.1029/2019JD030648

Rosenlof, K. and J. Holton (1993). Estimates of the stratospheric residual circulation using the downward control principle, J. Geophys. Res., 98, 10465-10479.

Sassen, K., Z. Wang, and D. Liu (2008). Global distribution of cirrus clouds from CloudSat/Cloud-Aerosol Lidar and Infrared Pathfinder Satellite Observations (CALIPSO) measurements, J. Geophys. Res., 113, D00A12, doi:10.1029/2008JD009972.

Schoeberl, M. R., et al. (2019). Water vapor, clouds, and saturation in the tropical tropopause layer. J. of Geophys. Res.: Atmospheres, 124, 3984–4003.

https://doi.org/ 10.1029/2018JD029849.

Schoeberl, M. R., Jensen, E. J., Pfister, L., Ueyama, R., Avery, M., & Dessler, A. E. (2018). Convective hydration of the upper troposphere and lower stratosphere. Journal of Geophysical Research: Atmospheres, 123, 4583–4593. https://doi.org/10.1029/ 2018JD028286

Schoeberl, M. R., E. J. Jensen, and S. Woods (2015). Gravity waves amplify upper tropospheric dehydration by clouds, Earth and Space Science, 2, 485–500, doi:10.1002/2015EA000127.

Schoeberl M. R., A. E. Dessler, T. Wang, M. A. Avery, and E. J. Jensen (2014). Cloud formation, convection, and stratospheric dehydration, Earth and Space Science, 1, 1–17, doi:10.1002/2014EA000014.

Schwartz, M.J., M.L. Santee, H.C. Pumphrey, G.L. Manney, A. Lambert, N.J. Livesey, L. Millan, J.L. Neu, W.G. Read, and F. Werner, Australian New Year's pyroCb impact on stratospheric composition, (2020). Geophys. Res. Lett., 47, e2020GL090831, doi:10.1029/2020GL090831

Solomon, S., Rosenlof, K. H., Portmann, R. W., Daniel, J. S., Davis, S. M., Sanford, T. J., and Plattner, G.-K. (2010). Contributions of stratospheric water vapor to decadal changes

in the rate of global warming, Science, 327, 1219–1223, doi:10.1126/science.1182488,.

Stevens, B. et al. (2019). DYAMOND: the DYnamics of the Atmospheric general circulation Modeled On Non-hydrostatic Domains, Progress in Earth and Planetary Science, 6:61,

https://doi.org/10.1186/s40645-019-0304-z

Thomason, L. W., L. R. Poole and T. Deshler (1997). A global climatology of stratospheric aerosol surface area density deduced from Stratospheric Aerosol and Gas Experiment II measurements: 1984-1994, J. Geophys. Res. , 102, 8967-8976.

Thomason, L. W., Moore, J. R., Pitts, M. C., Zawodny, J. M., and Chiou, E. W. (2010). An evaluation of the SAGE III version 4 aerosol extinction coefficient and water vapor data products, Atmos. Chem. Phys., 10, 2159–2173, https://doi.org/10.5194/acp-10-2159-2010

Thomason, L. W., and J.-P. Vernier (2013). Improved SAGE II cloud/aerosol categorization and

observations of the Asian tropopause aerosol layer:1989-2005, Atmos. Chem. Phys., 13, 4605–

4616.

Torres, O., Bhartia, P. K., Taha, G., Jethva, H., Das, S., Colarco, P., et al. (2020). Stratospheric injection of massive smoke plume from Canadian boreal fires in 2017 as seen by DSCOVR-EPIC, CALIOP, and OMPS-LP observations.

J. Geophys. Res. Atmos., 125, e2020JD032579. https://doi.org/10.1029/2020JD032579

Ueyama, R., E. Jensen, L. Pfister, M. Krämer, A. Afchine, and M. Schoeberl (2020). Impact of convectively detrained ice crystals on the humidity of the tropical tropopause layer in boreal winter, J. Geophys. Res. Atmos., 125, e2020JD032894.

Ueyama, R., E. J. Jensen, L. Pfister, and J.-E. Kim (2015). Dynamical, convective, and microphysical control on wintertime distributions of water vapor and clouds in the tropical tropopause layer, J. Geophys. Res. Atmos., 120, 10,483–10,500, doi:10.1002/2015JD023318.

Voigt, A., N. Albern, G. Papavasileiou, (2019). The atmospheric pathway of the cloud-radiative impact on the circulation response to global warming: Important and uncertain, J. Climate, 32, 3051-3067, DOI: https://doi.org/10.1175/JCLI-D-18-0810.1

Wang, T., and Dessler, A. E. (2012). Analysis of cirrus in the tropical tropopause layer from CALIPSO and MLS data: A water perspective, *J. Geophys. Res.*, 117, D04211, doi:10.1029/2011JD016442.

Wang, P-H., M.P. McCormick, L.R. Poole, W.P. Chu, G.K. Yue, G.S. Kent, K.M. Skeens (1994). Tropical high cloud characteristics derived from SAGE II extinction measurements,

Atmospheric Research, 34, 53-83, ISSN 0169-8095, https://doi.org/10.1016/0169-8095(94)90081-7.

Wang, P-H., P. Minnis, M. P. McCormick, G. S. Kent, and K. M. Skeens (1996). A 6-year climatology of cloud occurrence frequency from Stratospheric Aerosol and Gas Experiment lI observations (1985-1990), J. Geophys. Res, 101, 29407-29429.

Wang, P-H., M. P. McCormick, P. Minnis, G. S. Kent, G. K. Yue, and K. M. Skeens (1995), A method for estimating the vertical distribution of the SAGE II opaque cloud frequency, *Geophys. Res. Lett.*, 22, 243-246.

Wang, P.-H., Minnis, P., Wielicki, B. A., Wong, T., Cess, R. D., Zhang, M., Vann, L. B., and Kent, G. S. (2003). Characteristics of the 1997/1998 El Nino cloud distributions from SAGE II observations, J. Geophys. Res., 108, 4009, doi:10.1029/2002JD002501

Wang, T., D. Wu, J. Gong, V. Tsai (2019). Tropopause laminar cirrus and its role in the lower stratosphere total water budget, J. Geophys. Res. Atmospheres, https://doi.org/10.1029/2018JD029845

Wiensz, J.T., D. A. Degenstein, N. D. Lloyd, and A. E. Bourassa (2013). Retrieval of subvisual cirrus cloud optical thickness from limb-scatter measurements, Atmos. Meas. Tech, 6, 105-119, doi:10.5194/amt-6-105-2013

Winker, D. M., et al. (2010). The CALIPSO mission: A global 3D view of aerosols and clouds, Bull. Am. Meteorol. Soc., 91, 1211–1229, doi:10.1175/2010BAMS3009.1

Woods, S., Lawson, R. P., Jensen, E., Bui, T. P., Thornberry, T., Rollins, A., et al. (2018). Microphysical properties of tropical tropopause layer cirrus. Journal of Geophysical Research:

Atmospheres, 123. https://doi.org/ 10.1029/2017JD028068

Young, S. A., and M. A. Vaughan (2009). The retrieval of profiles of particulate extinction from Cloud-Aerosol Lidar Infrared Pathfinder Satellite Observations (CALIPSO) data: Algorithm

description, J. Atmos. Oceanic Technol., 26, 1105–1119, doi:10.1175/2008JTECHA1221.1

Young, S., M. Vaughan, A. Garnier, J. Tackett, J. Lambeth, and K. Powell, (2018). Extinction and optical depth retrievals for CALIPSO's Version 4 data release, Atmos. Meas. Tech., 11, 5701–5727, 2018 https://doi.org/10.5194/amt-11-5701-2018

Yu, P., S. M. Davis, O. B. Toon, R. W. Portmann, C. G. Bardeen, J. E. Barnes, H. Telg, C. Maloney and K. H. Rosenlof (2021). Persistent Stratospheric Warming due to 2019-20 Australian Wildfire Smoke, Geophysical Research Letters, 48, e2021GL092609. https://doi.org/10.1029/2021GL092609

Zhou, C., A. E. Dessler, M. D. Zelinka, P. Y ang , and T. Wang (2014). Cirrus feedback on interannual climate fluctuations, Geophys. Res. Lett., 41, 9166–9173, doi:10.1002/2014GL062095

Zhou, C., A. E. Dessler, M. D. Zelinka, P. Yang, and T. Wang (2014). Cirrus feedback on interannual climate fluctuations, Geophys. Res. Lett., 41, 9166–9173, doi:10.1002/2014GL062095.